Generating atmospheric turbulence using passive grids in an expansion test section of a wind tunnel

Vita, Giulio; Hemida, Hassan; Andrianne, Thomas; Baniotopoulos, Charalampos

DOI:
10.1016/j.jweia.2018.02.007

Generating atmospheric turbulence using passive grids in an expansion test section of a wind tunnel

Giulio Vita[1]*, Hassan Hemida[2], Thomas Andrianne[3], Charalampos Baniotopoulos[4]

Abstract. Generating atmospheric turbulence in wind tunnels is an important issue in the study of wind turbine aerodynamics. A turbulent inlet is usually generated using passive grids. However, to obtain an atmospheric-like flow field relatively large length scales (*L~30* cm) and high turbulence intensities (*I~15* %) need to be reproduced. In this work, the passive grid technique has been used in combination with a downstream expansion test section in order to investigate the generation of atmospheric like turbulence, with the possibility of varying both the turbulence intensity and the integral length scale of the flow field independently. Four passive grids with different mesh and bar sizes were used with four wind velocities and five downstream measurement positions. It was found that the flow field is isotropic and homogeneous for distances less than what is recommended in literature (*x/M~5*). The effect of the expansion on the turbulence characteristics is also investigated in detail for the first time. The study confirms that by adding an expansion test section it is possible to increase both turbulence intensity and integral length scale downstream from the grid with limited impact on the overall flow quality in terms of anisotropy and energy spectra.

1. Introduction

The generation of controlled statistics of turbulence at the inlet of wind tunnel tests is of paramount importance for many aerodynamic applications. Research on bluff body aerodynamics (Bearman and Morel, 1983; Nakamura et al., 1988), turbulence decay (Comte-Bellot and Corrsin, 1966), turbulence interaction noise (Kim et al., 2016) or wind energy (Sicot et al., 2008) requires Free Stream Turbulence (FST) with a rather faceted spectrum of length scales and turbulence intensities to be generated at the inlet. Several approaches can be used for this purpose, such as grid generated turbulence, thermal driven turbulence, the use of cross jets, and actuated foils. While each of these methods has some advantages and disadvantages, grid generated turbulence is considered as the most effective and reliable source of a turbulent inflow for wind tunnel testing (Batchelor, 1953; Hinze, 1975). At least three families of grids are found in the literature: passive, active, and fractal grids.
The use of a passive grid (PG) has been the elected technique of generating turbulence at the inlet of wind tunnel tests since the first pioneering works on turbulence decay (de Karman and Howarth, 1938; Simmons and Salter, 1934; Taylor, 1935). Grid turbulence is generated by the shedding of vortices downstream of bars. The upstream quiescent flow undergoes a transition to a homogeneous and isotropic turbulent flow, characterised with slow rotating vortices which roughly scale to the size of the bars of the grid $L_u \sim b$ (Davidson, 2004). Once the flow is fully developed, turbulence decay dominates the statistics. The rate of decay has been set by Baines and Peterson (1951) and Vickery

[1] Early Stage Researcher & PhD Student, Department of Civil Engineering, University of Birmingham, UK
[2] Senior Lecturer, Department of Civil Engineering, University of Birmingham, UK
[3] Head of Wind Tunnel Lab, Department of Aeronautics, Université de Liège, BE
[4] Professor, Department of Civil Engineering, University of Birmingham, UK

(1966) to *-5/7*, while Laneville (1973) has instead proposed a value of *-8/9*. Mohamed and LaRue (1990) pointed out that two distinct regions of the flow exist, namely the far-field region, where turbulence decay is the main feature of the flow, and the near-field region, where production and a strong effect of the initial conditions are present (George, 2012). All PGs undergo such an analogous behaviour. Circular rods or square bars, arranged in square meshed or parallel arrays as well as perforated plates are used to build PGs with a variety of details, sizes and materials. Their effects have been systematically addressed by Roach (1987). However, the main classification of PGs is based on the dependence of the downstream turbulence on the Reynolds number, which is predominantly dictated by the shape of bars. Circular rods have a wake pattern that varies greatly with the Reynolds number or their roughness, while blunt bars feature a given separation at sharp corners (Bearman and Morel, 1983). Square bars compared to rectangular ones are more Reynolds sensitive, as flow re-attachment occurs more easily, modifying their wake (Nakamura, 1993). Smoothing or trimming the corners of square or rectangular bars has a limited impact on the turbulence characteristics (Nakamura et al., 1988). Although the use of rectangular bars is discouraged by some authors (Hancock and Bradshaw, 1983), others did not encounter any significant issues (Bearman and Morel, 1983; Nakamura, 1993; Nakamura et al., 1988; Vickery, 1966). The bar typology can be associated with different concepts for the construction of grids: Bi-planar grids (two sets of parallel bars placed side-by-side); Mono-planar grids (two set of overlapping parallel bars); A single set of parallel bars, either vertical or horizontal. Hancock and Bradshaw (1983) found that a bi-planar grid is preferable as mono-planar grids produce a highly unsteady non-uniform flow, possibly because of the larger separated region behind each intersection. Bearman and Morel (1983) argued that the non-uniformity of the flow decays in a much faster way for mono-planar grids than that of the bi-planar grid. However, the two grid options generate a similar turbulent flow (Nakamura et al., 1988; Roach, 1987). Nevertheless, the effect of the detailing of the grid is no longer apparent when the turbulent flow is fully developed. At what distance this occurs is still debated in research (Isaza et al., 2014). A mesh distance of $x/M > 10$ is considered by many authors (Bearman and Morel, 1983; Gartshore, 1984; Laneville, 1973; Saathoff and Melbourne, 1997; Vickery, 1966), but it is arguable whether this indication is sufficient to assume an independence of statistics with respect to the chosen detailing of the grid (Frenkiel et al., 1979).

The active grid (AG) concept uses a number of winglets mounted on a series of shafts, which rotate to generate a highly turbulent isotropic flow downstream of the grid (Makita, 1991; Makita and Sassa, 1991). This complicated setup has been further developed (Brzek et al., 2009; Cal et al., 2010) to produce integral length scales in the order of the cross-section size of the wind tunnel $L_u \sim H$ (Mydlarski and Warhaft, 2006). The turbulence characteristics can be adjusted by altering the rotating speed of the winglet-shafts (Cekli and van de Water, 2010; Kang et al., 2003; Larssen and Devenport, 2011). AGs have also been successfully used recently in research on wind energy (Maldonado et al., 2015).

The fractal grid (FG) concept has been recently developed to produce higher turbulence intensities and integral length scales up to $L_u \sim H/10$ as well as limiting the distance from the grid at which the flow can be considered fully developed (Hurst and Vassilicos, 2007; Seoud and Vassilicos, 2007). A fractal grid of *Nth* order is created from a fractal generating pattern of complexity *S*, whose geometry is iterated *N* times. Mesh and bar sizes are varied accordingly. This technique is similar to that of the passive grid generation. However, a production region exists close to the grid where turbulence statistics develop toward a peak value. This does not occur for passive grids (Melina et al., 2016). The flow behind FGs resembles that of the near-field of passive grids. While the implementation of FGs for bluff body aerodynamics is being explored (Nedić and Vassilicos, 2015), PGs are more commonly used.

Thus far, many studies have investigated the effects of free stream turbulence for a variety of applications. However, only a few of them have attempted to address the effect of the turbulent statistics, taken independently of one another (Arie et al., 1981; Lee, 1975; Morenko and Fedyaev, 2017; Peyrin and Kondjoyan, 2002; Younis and Ting, 2012). If PG is the methodology of choice to generate inlet turbulence, a thorough study of the turbulence statistics at the inlet is sometimes only briefly mentioned, or omitted altogether. This might depend on the limited significance of the results, since low turbulence intensities (<5 %) are normally available for large integral length scales (>20 cm) (Roach, 1987), while in the atmosphere higher turbulence intensities (>15 %) are found (Antoniou et al., 1992; Kaimal et al., 1976). In order to achieve higher values for the turbulence intensity, the only possible way is to reduce the measuring distance from the grid, keeping the mesh and bar size sufficiently large to yield suitable length scales even close to the grid. However, the homogeneity and isotropy condition may not be achieved. It could be argued whether the distance limitation given in literature of $x/M>10$ could be re-formulated for those studies not aimed at turbulence decay. Roach (1987) has warned that such limitations might be overconservative, suggesting that a homogeneous and isotropic, although not fully decaying, flow might be found closer to the grid.

Nevertheless, turbulence statistics of grid turbulence show a deviation from the condition of isotropy. Comte-Bellot and Corrsin (1966) confirmed the validity of the exponential decay law of de Karman and Howarth (1938), however they used a slight contraction of the wind tunnel section to achieve turbulence intensity isotropy. Although the inhomogeneity caused by the contraction does not affect the energy transfer of the decay rate, it was noted that integral length scale isotropy is more difficult to obtain. Later, several works have introduced a contraction section downstream of the PG. While most studies about the effect of a contraction on turbulent flows focus on the design of wind tunnels (Uberoi, 1956), some more recent works (Bereketab et al., 2000; Mish and Devenport, 2006; Swalwell et al., 2004; Wang et al., 2014) apply a contraction to adjust the isotropy for the inlet of bluff body aerodynamics applications. However, this approach causes a damping of turbulence downstream of the contraction, which in turn does not guarantee isotropy condition to be met for all statistics (Kurian and Fransson, 2009). Together with contractions, also expansion test sections, or diffusers, are broadly used in wind tunnels. Diffusers are placed as exit sections downstream of the working section, to create a pressure rise. Wide-angle diffusers are also needed upstream to allow for a contraction to be placed at the inlet to obtain a desirable steady flow (Bradshaw and Pankhurst, 1964). A diffuser is usually placed downstream or upstream of fans, as they need to be 2-3 times larger than the test-section to achieve a high quality flow field (Mehta, 1979). Diffusers have been tested regarding the performance in recovering pressure with reference to free stream turbulence (Hoffmann, 1981), but to the knowledge of the authors their use as a mean of modifying turbulent inlet statistics in wind tunnel testing is not yet reported in literature.

This paper introduces a novel method of varying turbulence statistics at the inlet of wind tunnel tests using an expansion section. The literature review has clarified that the generation of an atmospheric-like inflow is a challenging issue in the investigation of the effect of turbulence on bluff body aerodynamics, especially in obtaining large integral length scale turbulence (L_u~0.3 m) combined with high turbulence intensity (I_u~15 %). In the following, the grid generated turbulent flow upstream and downstream of an expansion test section is investigated. The aim is to show the possibility of modulating the turbulent flow to enhance statistics, without compromising them in terms of isotropy and gaussianity. The possibility of varying independently the various statistics is also assessed to understand their compatibility with atmospheric turbulence. Thanks to a thorough study of the turbulence decay mechanism, a simple empirical relation is proposed to predict the turbulence statistics at the outlet of the expansion. In Section 2, the experimental setup is reported together with the methodology to calculate results presented in Section 3. The feasibility of using an expansion together with grid generated turbulence has been assessed with the study of turbulence decay, isotropy, gaussianity, and energy spectra, and conclusions are given in Section 4.

2. Methodology

2.1. Experimental setup

The experiments were carried out in the multi-disciplinary wind tunnel of the University of Liège. The wind tunnel was operated in closed-loop configuration. The *1.50* m high and *1.95* m wide aeronautical test section (TS1) has a total length of *5* m. The *4×4* m contraction at the inlet nozzle, together with a series of honeycomb and a series of fine-grid screens, allows a remarkably low turbulence level (*0.15* %). The flow is accelerated by the *440* kW, *2.8* m diameter rotor that can drive the flow at velocity between *1* m/s and *65* m/s in closed-loop configuration. Figure 1 shows a schematic of the test section. The *5* m long TS1 has a *5.1* m expansion to bind the aeronautical cross-section to the larger atmospheric boundary layer cross section TS2 which is *2.5* m wide and *1.8* m high. Therefore, a part of the TS2 section was also used for the measurements.

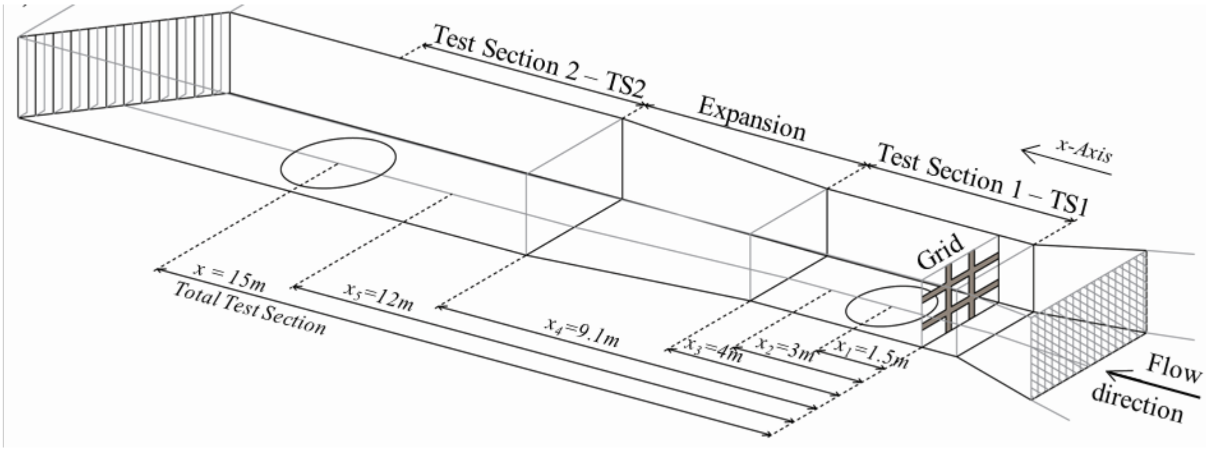

Figure 1. Experimental setup: the aeronautical Test Section (TS1) of the Wind Tunnel of the University of Liège

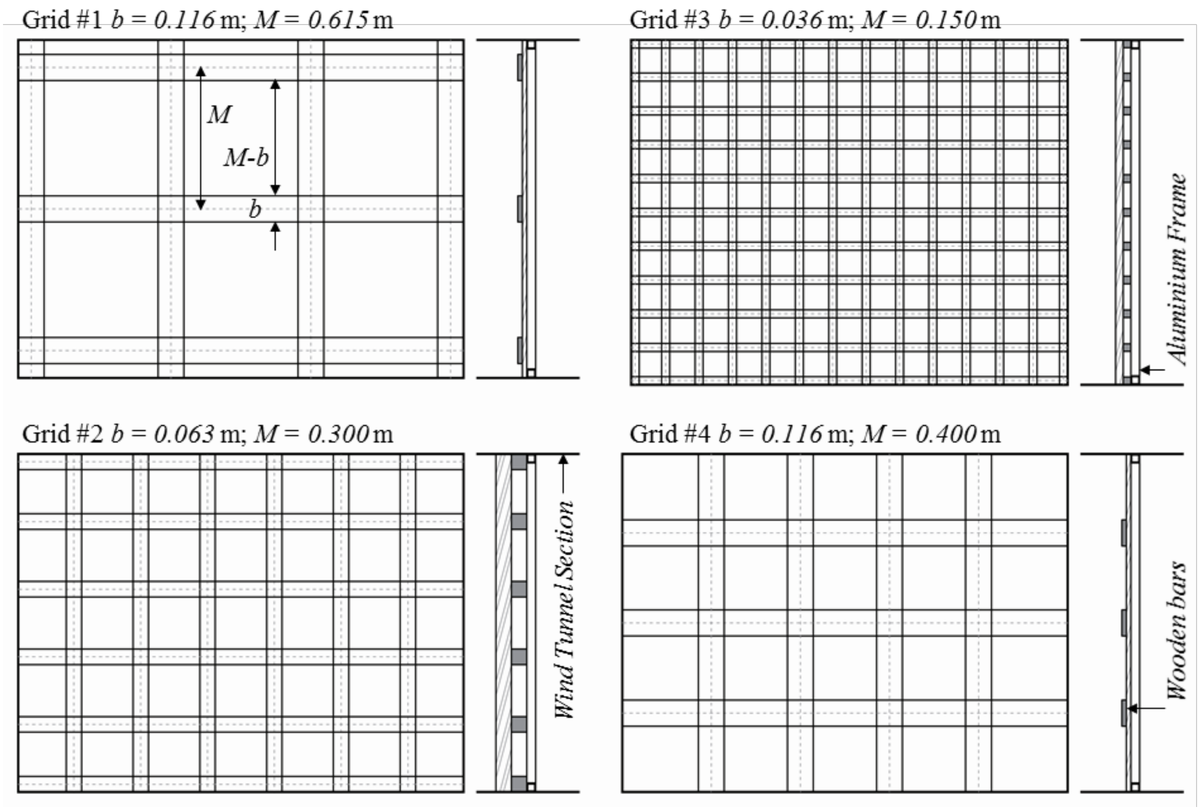

Figure 2. Schematic (front and side view) of the set of four grids #, with bar b and mesh M size.

2.2. Design of Passive Grids

The design of a turbulent inflow to be generated with a PG requires a careful choice of at least three parameters: the width b of the bars, the mesh size M (i.e. the distance between the centreline of the bars), and the downstream distance x to the grid (Figure 2 and Figure 3), where the measurements are performed. Vickery (1966) provides an indication for the optimal mesh size of $M = L/8$, where L is the length of the test section. The ratio b/M can be chosen based on the definition of grid drag (Laneville, 1973)

$$c_D = \frac{b/M\,(2\text{-}b/M)}{(1\text{-}b/M)^4} \quad (1).$$

Laneville (1973) recommends to keep c_D between 3 and 4. Consistently, Vickery (1966) suggested $c_D \sim 3.4$, while for Baines and Peterson (1951) $c_D > 3.4$. The grid drag is connected to the definition of porosity β (or its dual, solidity) by:

$$\beta = (1\text{-}b/M)^2 \quad (2)$$

Bearman and Morel (1983) advised a value of at least 0.5 for β, which is also confirmed by Nakamura et al. (1988) and Roach (1987). However, using $\beta=0.5$ leads to $c_D<2$, which is a more common value to be found in research on bluff body aerodynamics. Using these brief indications, Roach (1987) has given some guidelines for designing PGs based on fitting empirical constants to a large set of data, bar sizes and grids. However, the general validity of these guidelines is not assured, since conclusions were drawn from a limited set of wind tunnels. Nevertheless, simple design guidelines provide a useful tool for a preliminary estimation of the PG configurations. The empirical formulae derived by Roach (1987) are reported in Table 1 for turbulence intensities I_u and I_v, integral length scale L_u and Taylor microscale λ_u, where the subscripts u, v and w indicate respectively the stream-wise, horizontal and vertical components.

Table 1 Empirical relations for turbulence characteristics (after Roach, 1987)

Empirical expression	$I_u=A(x/b)^{-5/7}$	$I_v=AB(x/b)^{-5/7}$	$L_u/b=C(x/b)^{1/2}$	$\left(\frac{\lambda_u}{b}\right)^2=\frac{14F(x/b)}{Re_b}$
Constants	$A=1.13$	$B=0.89$	$C=0.20$	$F=1$ or $F=1.21$

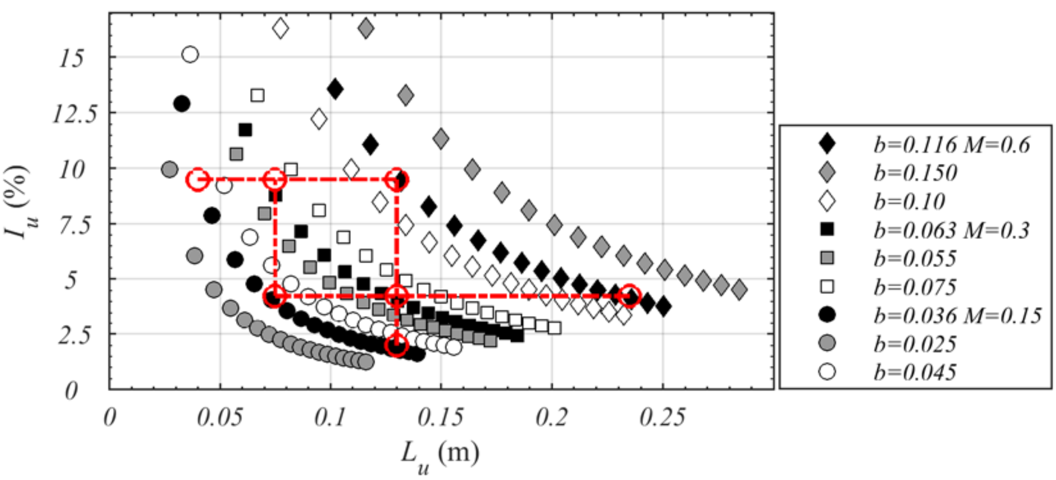

Figure 3. Preliminary design of the flow field. The symbols vary based on the different mesh size, while the filling is relevant to the chosen setup. The red lines and symbols indicate possible alignments for the statistics.

The set of grids have been designed by a preliminary choice of the target turbulent characteristics. Following this approach, several ratios of distances and grid sizes have been studied using the empirical formulae of Table 1. Despite this simplification, the setup is still rather complex. The proposed setup and the estimated length scales and intensities are indicated in Figure 3. Possible alignments of separately varied statistics are indicated (in red). It is evident how difficult can be to achieve L_u*~0.25* m together with I_u*~10-15* %. Only a set of three grids is provided here, while in the final experiment a set of four bi-planar square PGs is used.

The geometry and the turbulent statistics for the different grids are reported in Table 2. All results in the table refer to the distance of *x/M=10*, except for grid #1. All grids are placed in the same position *x=0*, i.e. at the inlet of TS1, without the use of any downstream contraction.

Table 2 Geometry of grids as shown in Figure 2(b)
with turbulence statistics at x/M=10 (x/M=6.5 for grid #1) and U_r*=15m/s.*

Grid	*b* [m]	*M* [m]	*M/b* [-]	*β* [-]	C_d [-]	*x/M* [-]	I_u [%]	L_u/b [-]	λ_u/b [-]	I_u/I_v ~1	L_u/L_v ~2	λ_u/λ_v $\sim\sqrt{2}$
#1	0.116	0.615	5.30	0.66	0.79	6.5	15.0	1.51	0.43	1.22	2.46	1.412
#2	0.063	0.30	4.76	0.62	0.97	10	8.35	1.81	0.68	1.14	2.13	1.320
#3	0.036	0.15	4.17	0.58	1.27	10	9.0	1.84	0.91	1.19	1.86	1.135
#4	0.116	0.4	3.45	0.5	1.95	10	11.0	1.39	0.32	1.2	1.81	1.0

A set of wooden bars have been overlapped in a bi-planar array and fixed firmly to an aluminium frame screwed to the inlet of TS1 Figure 2. The flow has been measured at 5 different positions, as indicated in Table 3, which have been shifted to respect the requirement of *x/M>5*.

Table 3 Position of measurements and mesh distance.

Position reference	*x* (m)	*x/M* #1	*x/M* #2	*x/M* #3	*x/M* #4
x_1	1.5	-	5	10	-
x_2	3	4.8	10	20	7.5
x_3	4	6.5	13.34	26.67	10
x_4	9.1	14.8	30.34	60.67	22.75
x_5	11.1	-	-	-	30

A total number of *15* measurements have been made for *4* different rotor wind speeds U_r, for a total of *60* tests. The different sets of grids are shown in Figure 2. The name of the grids and their different mesh sizes are also represented. The velocity measurements have been performed at the half-height of the wind tunnel $h = 0.74$ m. Measurements have been also made at the additional height of $h=1.07$ m to briefly assess the uniformity of the flow. This adds up to *9×4* tests for a total number of *96* tests.

Measurements have been made using a dynamic multi-hole pressure probe (Cobra Probe by Turbulent Flow Instrumentation inc., TFI), which allows the measurement of the three components of flow velocity from *2* to *100* m/s ±*1* m/s within a flow angle of ±*45* deg with a sampling frequency of up to *2* kHz. A proprietary software (TFI Device Control) is used as a data acquisition system (A/D card) to operate the probe. The sampling frequency chosen for this experiment is *500* Hz over a duration of the recorded signal of $t = 60.0$ s. This gives a range of non-dimensional time units, *Ut/b*, between *1,000* and *33,500*, where *U* is the average velocity, *b* the bar width and *t* the duration of the signal. The wind speed has been varied from *5* to *20* m/s in four steps.

2.3. Calculation of statistics

The turbulent flow is described using both one- and two-point statistics for the stream-wise, horizontal and vertical components of velocity u, v and w. The fluctuating velocity u is calculated using the Reynolds decomposition $u = u(t) - U$, where $u(t)$ is the velocity realisation as measured, and $U = \overline{u(t)}$ is the mean velocity. One-point statistics include the statistical moments, such as the variance $\overline{u^2}$, the standard deviation $\sqrt{\overline{u^2}}$, the skewness $S_u = \overline{u^3}/\left(\overline{u^2}\right)^{3/2}$, the flatness (or kurtosis) $K_u = \overline{u^4}/\left(\overline{u^2}\right)^2$, and the excess kurtosis $\gamma_u = K_u - 3$. The energy in a turbulent flow field can be assessed from $\sqrt{\overline{u^2}}$, in the form of turbulence intensity:

$$I_u = \sqrt{\overline{u^2}}/U\ ;\ I_v = \sqrt{\overline{v^2}}/U\ ;\ I_w = \sqrt{\overline{w^2}}/U \qquad (3).$$

The integral length scale L_u is a measure of the largest energy containing vortices. L_u can be estimated from the autocorrelation coefficient $\rho(\tau) = R_{uu}(\tau)/\overline{u^2}$, where $R_{uu}(\tau) = \overline{u(t)u(t+\tau)}$ is the autocorrelation function, and τ is the time lag. In this case $L_u = UT_u$ where T_u is the integral time scale, obtained from the area subtended by the $\rho(\tau)$ curve, which is usually approximated with:

$$L_u = U\int_0^{\tau_0} \rho(\tau)d\tau \qquad (4),$$

where $\rho(\tau_0) = 0$. T_u can also be estimated using a simplified relation, where $\rho(T_u) = 1/e$ (Conan, 2012). The power spectral density or spectrum E_u is defined from the Wiener-Khintchine theorem:

$$E_u(n) = \frac{1}{2\pi}\int_{-\infty}^{\infty} e^{-in\tau}R_{uu}(\tau)d\tau \qquad (5),$$

where n is the frequency. L_u can be estimated using the best fit of E_u with the von Kármán formula:

$$E_u(n) = \frac{4L_u\overline{u^2}/U}{(1+70.8(nL_u/U)^2)^{5/6}} \qquad (6),$$

which only applies for homogeneous isotropic turbulence. All approaches yield results with a relative error <15 %, hence the $1/e$ rule is used in the following.

Since turbulence is composed of a broad band of frequencies, it is important to have also a reference to the energy distribution for a given frequency band. The Taylor microscale λ_u is commonly used for this purpose, as it represents the largest dissipative length scale. λ_u can be found from the dissipation rate ε:

$$\varepsilon = 15\nu\int_0^{\infty} \kappa^2 E_u(\kappa)\, d\kappa \qquad (7),$$

where $\kappa = 2\pi n/U$ is the wave number and $E_u(\kappa) = UE_u(n)/2\pi$ is the wave number power spectral density. In isotropic turbulence, the following relation applies:

$$\frac{1}{\lambda_u^2} = \frac{\varepsilon}{15\nu\overline{u^2}} = \frac{1}{\overline{u^2}}\int_0^{\infty} \kappa^2 E_u(\kappa)d\kappa = \frac{2\pi^2}{U^2\overline{u^2}}\int n^2 E_u\, dn \qquad (8),$$

where E_u might represent either the computed or the fitted spectrum. However, Roach (1987) warns that in order to obtain an accurate estimation of ε using the relations which are valid for homogeneous isotropic turbulence, a sampling rate of 10-100 kHz has to be chosen when collecting the data, which is often unpractical. Alternatively, ε can be estimated fitting the spectrum with its inertial sub-range $E_u(\kappa) = C\varepsilon^{2/3}\kappa^{-5/3}$ (Pope, 2000). The multiplicative constant is $C = 18/55\, C_\kappa \sim 0.49$ for the stream-wise spectrum and $C = 24/55\, C_\kappa \sim 0.65$ for the horizontal spectrum. $C_\kappa \sim 1.5$ is the Kolmogorov universal constant (Sreenivasan, 1995). Another way of calculating λ_u is using the Taylor's hypothesis and the intercept of $\rho(\tau)$ with a parabola at the origin (Pope, 2000):

$$\lambda_u^2 = \overline{u^2}/\overline{(\partial u/\partial x)^2} = U^2\overline{u^2}/\overline{(du/dt)^2} \qquad (9).$$

Both Equations 8 and 9 are estimations based on assumptions, and a careful study should be undertaken for the most suitable approach. In this work, Equation 9 has been chosen for the calculation of λ_u. The smallest turbulent motion, named Kolmogorov microscale η, is another useful value which is defined from the dissipation rate ε:

$$\eta = \left(\nu^3/\varepsilon\right)^{1/4} \tag{10}$$

The transversal and horizontal integral and Taylor length scales, respectively L_v, L_w, λ_v, and λ_w, are calculated with formulae, analogous to the previously introduced ones (Hinze, 1975; Pope, 2000). Further conclusions on the behaviour of a turbulent flow can be drawn by calculating the Reynolds stress tensor $\overline{u_i u_j}$. In particular, the tensor a_{ij}, first introduced by Lumley (1979), gives a measure of the deviation of the flow field from the isotropy definition of $\overline{u_i u_j} = 1/3\, q^2 \delta_{ij}$, where $q^2 = 2k = \overline{u_k u_k}$ is twice the turbulent kinetic energy. The anisotropy tensor a_{ij} is defined by

$$a_{ij} = \frac{\overline{u_i u_j}}{q^2} - \frac{1}{3}\delta_{ij} \tag{11}$$

The second and third invariant of a_{ij}, respectively $II_a = a_{ij}a_{ji}$ and $III_a = a_{ij}a_{jk}a_{ki}$, are used to define an anisotropy invariant map, which defines precisely the rate and the typology of turbulent flow (Jovanović, 2004), varying from pure isotropy $II_a = III_a = 0$ to one-component turbulence. This map has confirmed that grid turbulence yields a highly isotropic flow field (Geyer et al., 2016).

3. *Results and discussion*

Results are presented in this section considering the following topics of investigation: the decay of turbulence, the isotropy and the gaussianity of the flow, and the spectrum of statistics varied separately one another. Results are presented in scatter plots and the symbols used to refer to the different parameters are introduced in Table 4. Four different symbols are used indicating the four different grids and the colour represents either the wind speed used, or the distance referred to the expansion test section, when wind speed does not affect the statistics. In Table 4, the legend for results is reported.

Table 4 Legend for results

Grid	Symbols	Wind Speed u_r (m/s)	Distance
#1	+	**5**	***x/M*** $\le$ ***10***
#2	□	**10**	***x*** $\ge$ ***9.1*** **m**
#3	○	**15**	***x/M >10*** ∪
#4	◇	**20**	***x<9.1*** **m**

Results are plotted against the distance from the grid x. In literature, x is often translated into mesh distance x/M or Reynolds mesh distance $x/M\ 1/Re_M$ first introduced by Comte-Bellot and Corrsin (1966). The bar size b can be also used to define x/b or $x/b\ 1/Re_b$, however results are better fitted using the mesh distance. The mesh Reynolds number reads $Re_M = UM/\nu$, and it highlights any dependence from the wind speed. Another useful parameter is the turbulent Reynolds number, which can be defined using λ_u or L_u, which yield $Re_\lambda = \sqrt{\overline{u^2}}\lambda_u/\nu$ and $Re_\Lambda = \sqrt{\overline{u^2}}L_u/\nu$, respectively. Re_λ and Re_Λ are used to underline the role of dissipation in the development of statistics. Whenever suitable, data is fitted with the approach used in von Kármán and Howarth (1938) using the formula $f(x) = A\,x^p$.

3.1. Turbulence Decay

The decay of turbulence is shown in Figure 4 a) and b), and Figure 5 a) and b) in terms of I_u, L_u/M, λ_u/M, and η/M, respectively. The data is plotted along with the predictive formulae reported in Table 1, which have been converted to the mesh distance. It has been found that the data collapses better using *x/M* rather than *x/b*. The empirical formulae have also been compared with the least square fit of the data.

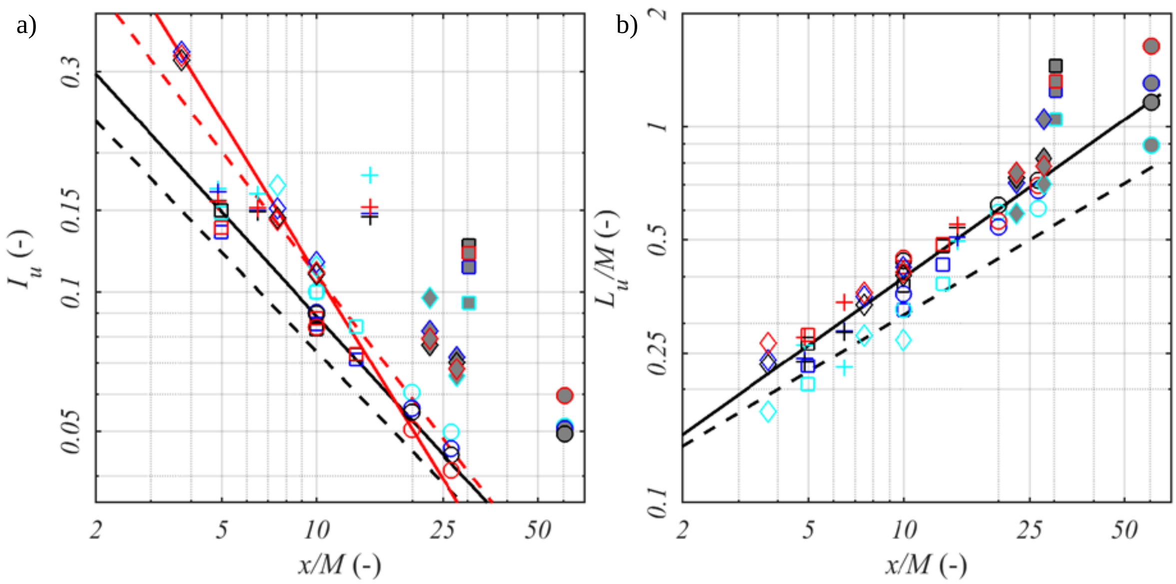

Figure 4 a) Turbulence Intensity decay with empirical fitting after Roach (1987) for grids #2 and #3 (- -) and after Laneville (1979) for grid #4 (- -). Least Square fitting of data is also provided for grids #2 and #3 (—) and grid #4 (—) as detailed in the text. b) Integral length scale decay with least square (—) and empirical fitting after Roach (1987) (- -) as detailed in the text. Markers are filled with a grey hatch if $x \geq 9.1$ m *and coloured after wind speed (Table 4).*

In Figure 4 a), the decay of I_u is plotted against the mesh distance *x/M*. Turbulence Intensity decays in a similar way for grids #2 and #3. The empirical formula given by Roach (1987) is close to the least square fit of the data $I_u = 0.5(x/M)^{-3/4}$. Grid #4 shows a similar behaviour, although I_u decays faster. The least square fit of the data $I_u = 1.41(x/M)^{-1.11}$ is closer to the formula $I_u = 2.54(x/b)^{-8/9}$ given by Laneville (1979). This difference in the behaviour seems to depend on the porosity β, respectively *0.62* and *0.58* for grids #2 and #3, and *0.50* for grid #4. Grid #1 shows a rather different behaviour, and a fit of the data reads $I_u = 0.2(x/M)^{-1}$, which is not plotted in Figure 4 a). A likely explanation for this may be the large size of the mesh compared to the wind tunnel section, which in turn causes the mean flow to be highly non-uniform. This is the reason for the inclusion of grid #4, in the experimental setup.

In Figure 4 b), the decay of L_u is plotted against *x/M*. In this case all grids behave consistently, and the fit of the data yields $L_u/M = 0.1(x/M)^{3/5}$, while the empirical formula given by Roach (1987) slightly underestimates L_u/M. In Figure 4, data is coloured after wind speed to highlight possible Reynolds effects. All results behave consistently for every wind speed, and only a small scatter of the data is noticeable for $U_r = 5$ m/s (data in cyan in Figure 4). This is possibly due to the limitations of Cobra probes in measuring velocities ~*2* m/s, therefore this velocity range is eliminated in the next figures.

The Taylor λ_u/M and Kolmogorov η/M microscales are plotted in Figure 5 a) and b), respectively. The empirical formulae overestimate λ_u/M when F is taken as given in Table 1, i.e. $F=1$ for isotropic turbulence or $F=1.21$ otherwise. A formula which fits all grids at all distances for this setup is $\lambda_u/M=(14\ \ 3/2\ \ x/M\,1/Re_M)^{3/5}$. In the same way, η/M can be accurately predicted for all data using the formula $\eta/M=0.8(x/M\,1/Re_M)^{1/2}$, which holds for homogeneous turbulence (Pope, 2000).

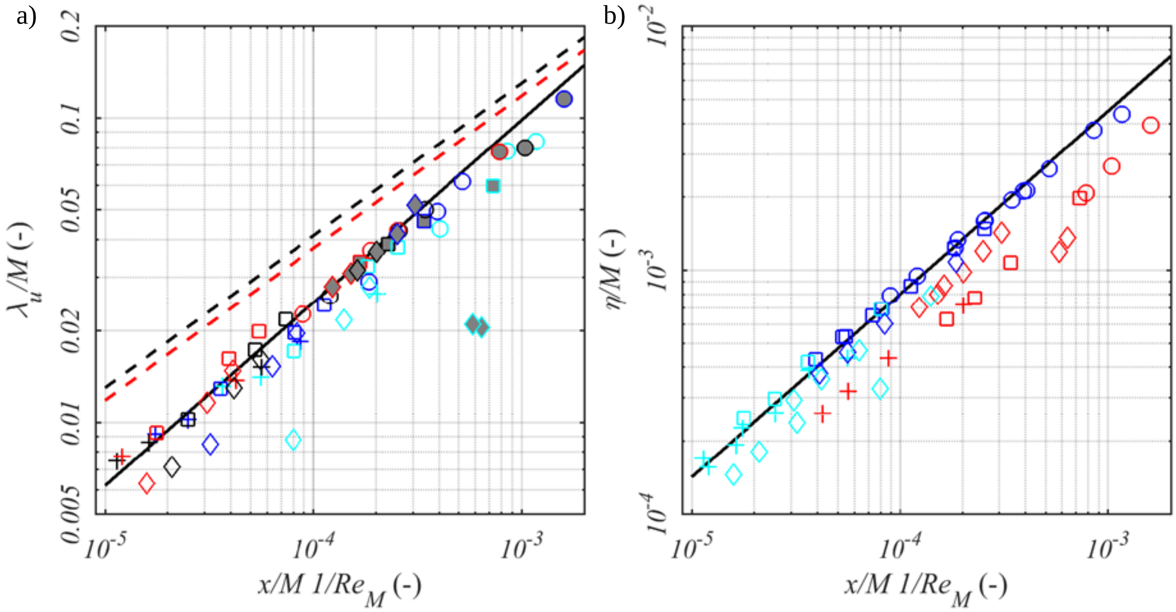

Figure 5 a) Taylor microscale decayand c) Taylor microscale against distance, with empirical fit as detailed in and b) Kolmogorov the text (Table 1) (—,- -). Colours after wind speed (Table 4). a) Turbulence Intensity decay with empirical fitting after Roach (1987) for grids #2 and #3 (- -) and after Laneville (1979) for grid #4 (- -). Least Square fitting of data is also provided for grids #2 and #3 (—) and grid #4 (—) as detailed in the text. b) Integral length scale decay with least square (—) and empirical fitting after Roach (1987) (- -) as detailed in the text. Markers are filled with a grey hatch if $x\geq 9.1$ m *and coloured after wind speed (Table 4).*

The behaviour of the length scale decay can be also interpreted with Figure 6 also, where the turbulent Reynolds numbers Re_Λ and Re_λ are plotted against $x/M\,1/Re_M$. All data taken at $x\leq 4$ m is fitted by $Re_\lambda=6.97(x/M\,1/Re_M)^{-0.38}$ and $Re_\Lambda=5.6(x/M\,1/Re_M)^{-0.72}$, regardless of distance or grid typology. Re_λ is very close to the results of Kurian and Fransson (2009), although they used grids with different bar shapes, while Re_Λ seems to converge towards their fit only at highest mesh distances. This confirms that the behaviour of the small scales has rather universal properties, which are independent of the initial conditions in which turbulence is created. The decay of the large scales seems to vary with the typology of the grid, at least for $5\leq x/M\leq 10$, but the decay law seems not to depend on the porosity of the grid.

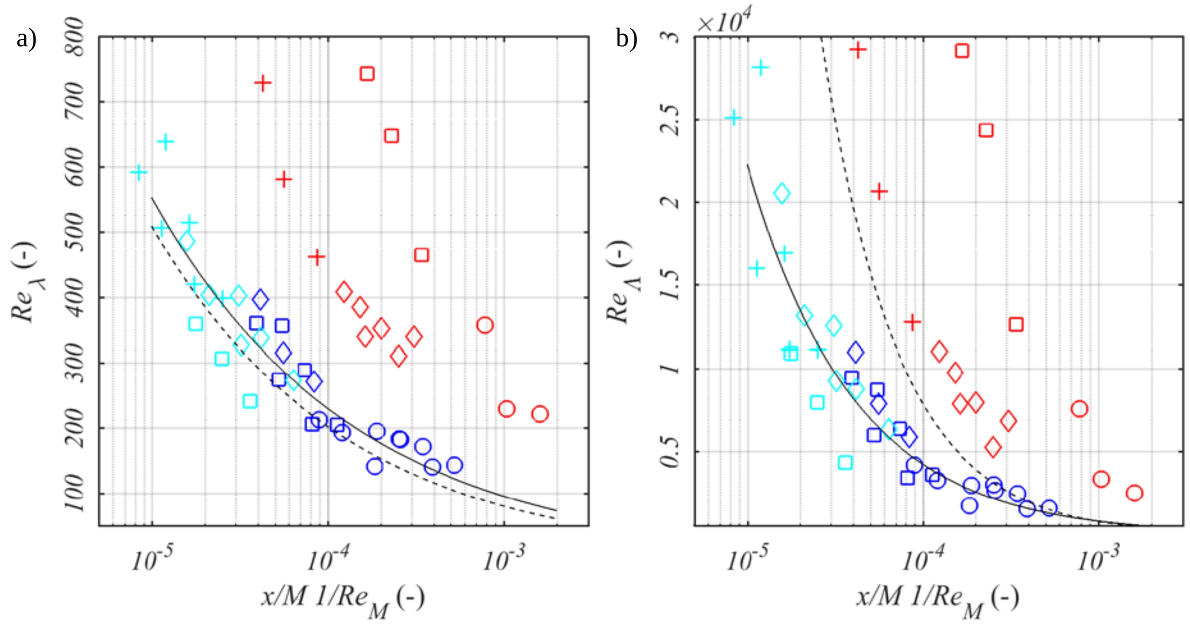

Figure 6 Turbulent Reynolds number relative to a) Taylor and b) integral scale against mesh distance, with fit of data (—) and fit by Kurian and Fransson (2009) (- -). Colours after distance (Table 4).

The ratio of integral and Taylor length scale, as shown in Figure 7 a), is proportional to the local turbulent Reynolds number Re_λ, with a proportionality coefficient of $C\sim 0.08$. Isaza et al. (2014) argue that $L_u/\lambda_u \propto Re_\lambda$ means that the data is measured in the far-field region of the flow, where only dissipation takes place and the effect of initial conditions posed by the construction of the grids have vanished. The constant of proportionality is given by $C= C_\varepsilon/K$ where $C_\varepsilon = \varepsilon L_u/S_u$ and K is a fitting constant. No effect of the different wind speeds is noticeable. Therefore, data is coloured based on the distance to the grid.

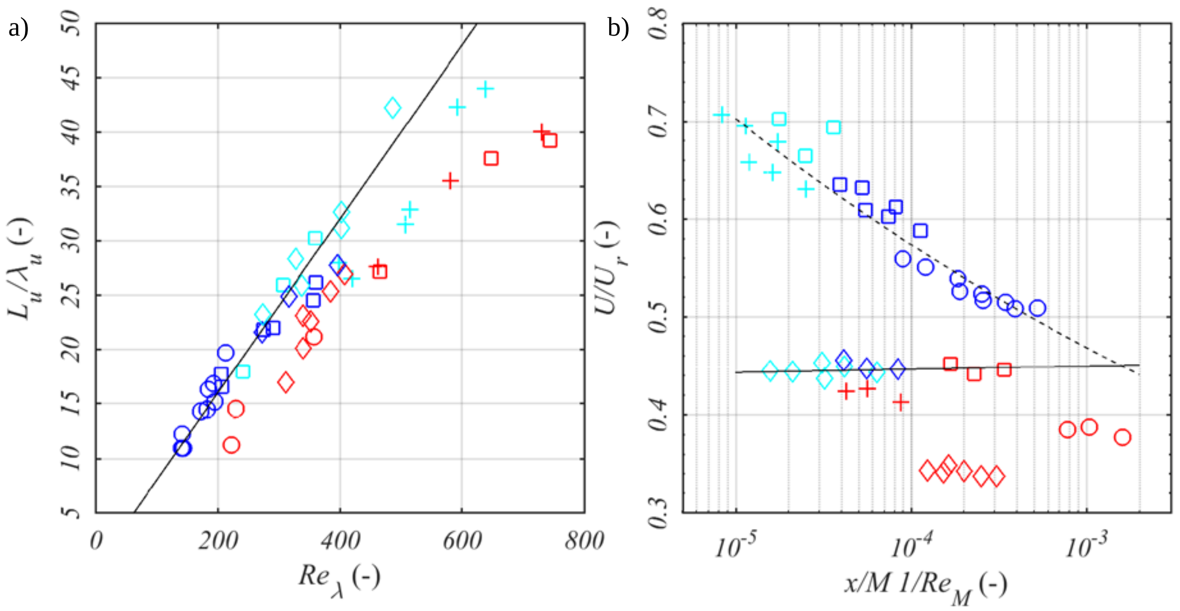

Figure 7. a) Integral and Taylor scale ratio dependence on the turbulent Reynolds number, with fit relation after Isaza et al. (2014) (—); b) Mean velocity ratio against mesh distance, with least square fit for grids #1, #2, and #3 (- -), and for grid #4 (—). Colours after distance (Table 4).

In Figure 4, Figure 5, Figure 6 and Figure 7, some data deviate from the empirical formulae in an apparent scatter. This is marked with a grey hatch in Figure 4 a) and b), and Figure 5 a). All the measurements which show this behaviour are taken at $x \geq 9.1$ m, i.e. at the outlet of the expansion test section of the wind tunnel of Liège. At $x \geq 9.1$ m, I_u recovers to values measured closer to the grid, while L_u increases with respect of what expected for such a setup. The increase rate of λ_u is comparable for all grids, unlike the other statistics. This confirms that dissipation is a phenomenon which exclusively depends on the Reynolds regime of the flow. Remarkably, the expansion has a very limited effect on the decay rate of λ_u, since the non-dimensional plot shows that the data is only affected by the Reynolds number, and this confirms that λ_u is extremely susceptible to changes in the wind speed. In Figure 6, the effect of the expansion is more visible, as data taken at $x \geq 9.1$ m is shifted from the empirical fit. Unlike data taken upstream to the expansion, a different slope is noticeable for different grid typologies. This could be explained with a definition of a parameter $x_L = 4/M$, where $x = 4$ m is the distance from the grid of the inlet of the expansion section, which reads $x_L = 6.50$, 13.34, 26.67, and 10 for grid #1, #2, #3, and #4, respectively. x_L represents the state of the flow at which the expansion section is encountered, which varies with the geometry of the grid. Turbulence generated by grids #2 and #3 encounters the expansion inlet for $x/M > 10$, unlike grids #1 and #4, and a different effect on the decay mechanism is expected.

The effect of the expansion on the turbulent flow field can be explained looking at the mean flow evolution with distance. In the investigation of turbulence decay, passive grids are designed to limit any gradients in the mean velocity so that only dissipative phenomena take place (George, 1992). However, this is achieved when any production process has vanished, i.e. at $x/M >> 10$. At these distances turbulence characteristics are not representative of atmospheric turbulence, and distances of $x/M \sim 10$ are most commonly found in research on bluff body aerodynamics. In this region, a change in the mean flow cannot be ruled out in principle. The change of the mean flow with distance is plotted in Figure 7 b). The mean velocity taken at the centreline of the wind tunnel U is divided by the reference wind speed U_r as given in Table 4. Besides the uniform case, the mean flow profile might resemble that of a jet or a wake, depending on the porosity of the grid. For self-preserving jets, an inversely proportional relation is defined: $U/U_r = C_U(x/M)^{-1}$ (Hussein et al., 1994). It is therefore reasonable to assume a relation of the type $U/U_r = C_U(x/M \;\; 1/Re_M)^n$ for grid generated turbulence, where C_U and n vary with the grid geometry (Pope, 2000). In this work, the fitting coefficients read $C_U = 0.25$ and $n = -0.09$ for grids #1, #2 and #3, and $C_U = 0.45$ and $n = 0.03$ for grid #4. For $n < 0$ the mean flow resembles a jet, while for $n > 0$ a wake-like profile is present. Therefore, the flow regime which is created is strongly affected by the initial conditions, and it seems that a lower porosity is beneficial in obtaining a more uniform flow. Nevertheless, the effect of the expansion on the mean flow might help understanding its effect on the turbulence decay. In Figure 7 b), a sudden drop in the mean velocity occurs at $x = 9.1$ m (data in red). The Venturi effect which occurs due to the change in the cross-section causes the mean velocity to decrease, and the turbulent vortices to stretch. Results presented in this Section do not show different behaviours for different Reynolds regimes, and the turbulence decay only depends on distance.

The effect of the expansion on grid generated turbulence seems to be limited to the rate of decay of turbulence, due to the changes occurring in the mean flow. Little effect is noticed on the small scales, confirming that dissipation is only affected by the Reynolds regime and not the initial conditions in which turbulence is created, namely the geometry of the grid.

3.2. Isotropy

The isotropy of a turbulent flow field can be assessed through turbulence intensity (Comte-Bellot and Corrsin, 1966), Taylor microscale and integral length scale (Roach, 1987), or a more comprehensive approach, such as the anisotropy invariant map (Banerjee et al., 2007).

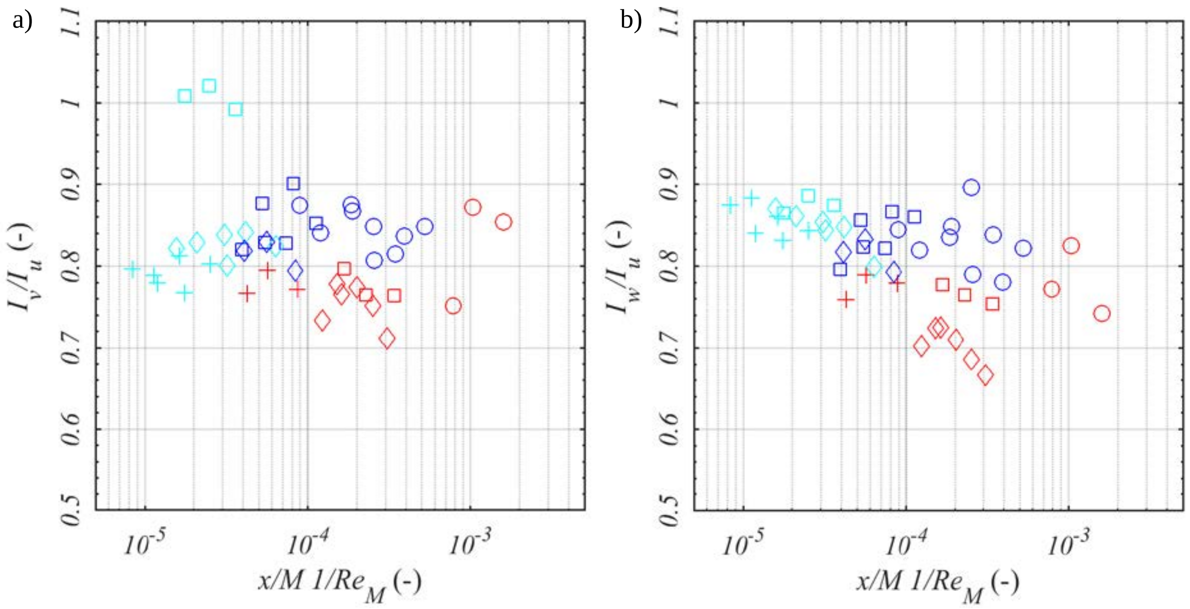

Figure 8 Turbulence Intensity anisotropy, a) horizontal and b) vertical component against non-dimensional mesh distance in logarithmic scale. Colours after distance (Table 4).

The isotropy of turbulence intensity is defined as the ratio of the standard deviation for the different velocity components, i.e. $I_v/I_u \approx I_w/I_u \approx 1$. The isotropy of turbulence intensity is illustrated in Figure 8 a) and b) against *x/M* $1/Re_M$. for both the horizontal and vertical component, *v* and *w*. The data show that distance does not improve isotropy substantially. Isotropy reaches ≈ *80* % for I_u/I_v and ≈ *90* % for I_u/I_w already relatively close to the grids, around *x/M~5*.

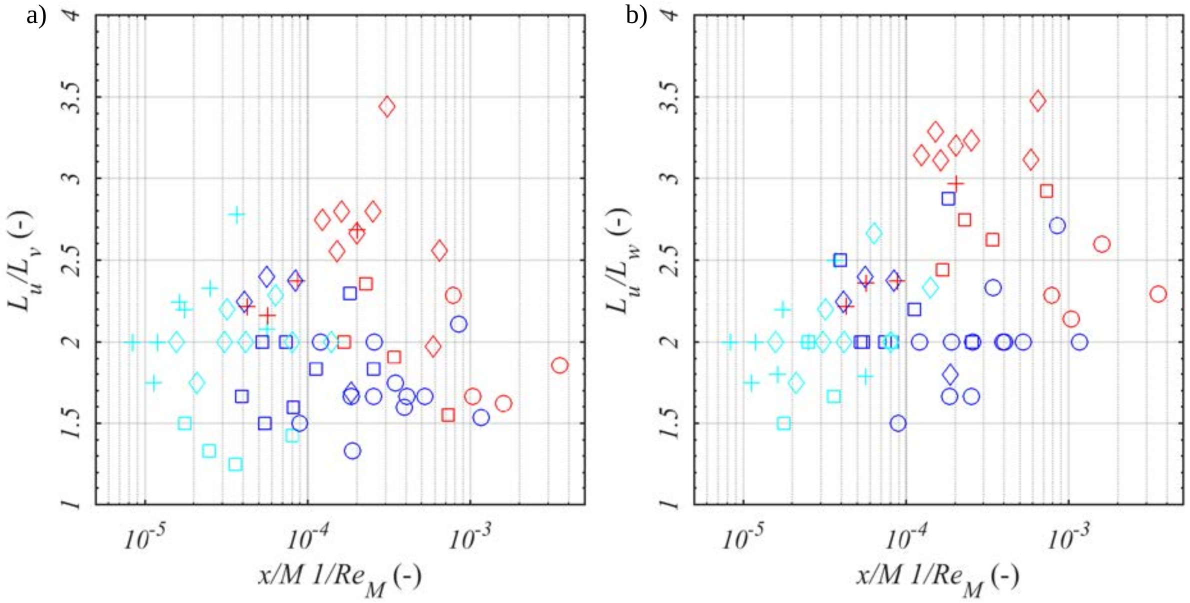

Figure 9 Integral length scale anisotropy for a) horizontal and b) vertical component against mesh distance. Colours after distance (Table 4).

The integral length scale isotropy condition reads $L_u/L_v \approx L_u/L_w \approx 2$. Both in Figure 9 a) and b), the isotropy rates L_u/L_v and L_u/L_w are very close to the theoretical condition for most data at around *x/M~10*.

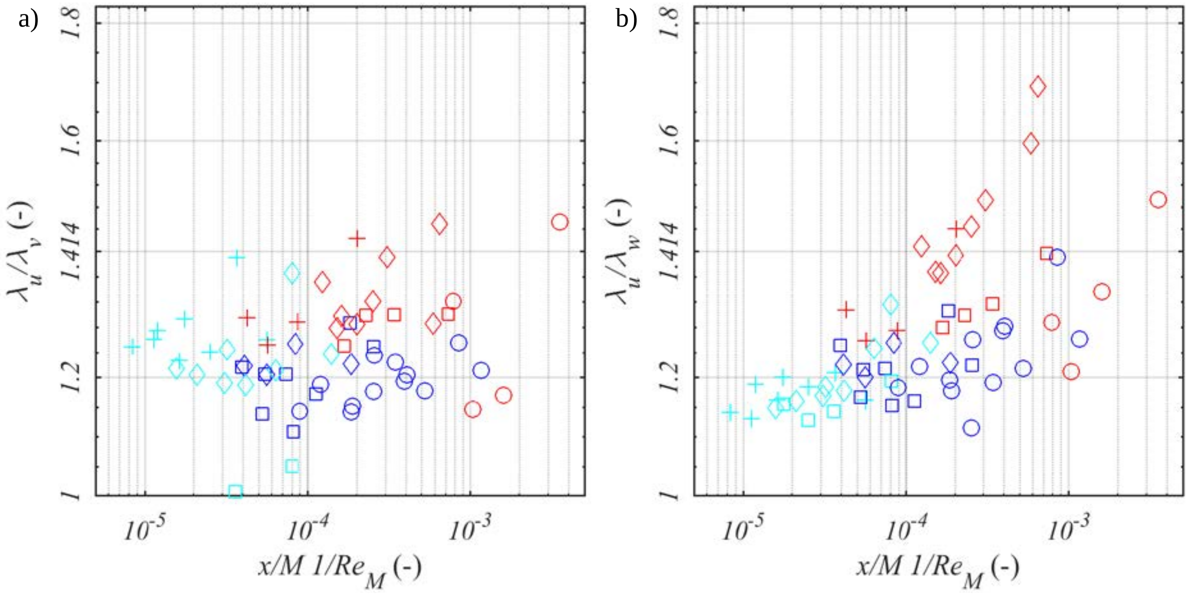

Figure 10 Taylor microscale anisotropy for a) horizontal and b) vertical component against mesh distance. Colours after distance (Table 4).

The isotropy condition for the Taylor microscale reads $\lambda_u/\lambda_v \approx \lambda_u/\lambda_w \approx \sqrt{2} \approx 1.414$, and it is plotted in Figure 10 against *x/M* 1/Re_M. Most data show a value of around *~1.2* for both components regardless of the distance from the grid.

It is rather difficult to draw conclusions on the effect of the expansion on the isotropy of the flow from Figure 8, Figure 9, and Figure 10, as results seems to contradict each another. The anisotropy of I_u seems to confirm that the expansion increases the anisotropy. This increase seems stronger for L_u as most data measured at $x \geq 9.1$ m deviates significantly from *2*. However, the expansion seems to improve the isotropy when looking at λ_u. Therefore, no convincing trends are found using the ratio of the different components of the statistics. Nevertheless, the results shown in Figure 8, 9 and Figure 10 are aligned to results found in literature for grid turbulence measured at distances *x/M>10*. Kurian and Fransson, (2009) have found good level of isotropy for *x/M >30*, however this longer distance can be due to the bar type used in the measurements (woven metal wires). Nevertheless, high isotropy has been observed for large wind tunnel configurations, for high (Kistler and Vrebalovich, 2006) and low Reynolds numbers (Wang et al., 2014), as well as for small wind tunnel configurations (Laneville, 1973). However, only few studies investigated distances *x/M<10* with regard to the isotropy of the flow, as the estimation of the difference in the decay rate from the near- and far-field region is most commonly considered (Mohamed and Larue, 1990).

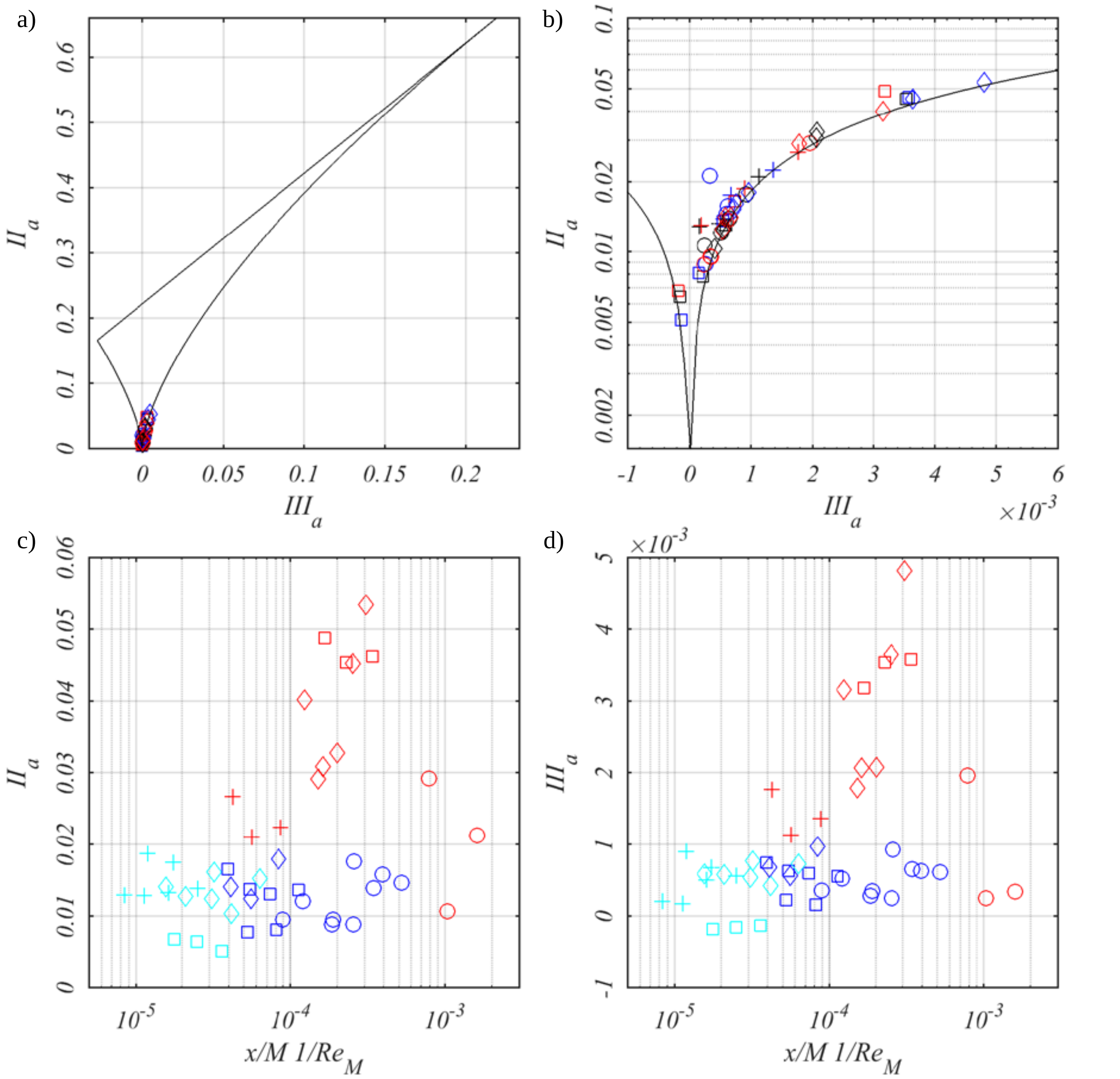

Figure 11 a) Anisotropy invariant map; b) zoom close to the isotropy condition. c) Second and d) third invariant plotted against x. Colours after a), b) wind speed and c), d) distance (Table 4).

A more comprehensive view of the anisotropy rate of the flow is given by considering the second II_a and third III_a invariants of the a_{ij} tensor, as defined in Equation (11). An anisotropy invariant map is shown in Figure 11 a) and b). To understand the effect of the distance on the anisotropy, II_a and III_a are plotted separately against the mesh distance in Figure 11 c) and d). A very good rate of isotropy is found for all grids, regardless of distance, as the invariants of the data taken at $x \leq 4$ m are close to the condition of perfect isotropy, $II_a = III_a = 0$, this is also true for $x/M \sim 5\text{-}10$, which confirms that a non-uniform flow field might still present highly isotropic turbulence. In Figure 11 c) and d), data taken at $x \geq 9.1$ m (shown in red) diverges from the isotropy condition, being closer to mildly axisymmetric turbulence, a condition which is typical for vortices being stretched as they are forced through an expansion (or a contraction) (Batchelor, 1953). It is interesting to note that for the empty wind tunnel $II_a = 0.5$ and $III_a = 0.15$, which holds for highly axisymmetric turbulence.

The flow field shows a high isotropy closer to the grid than what is commonly suggested in literature, at $x/M \sim 5$ instead of $x/M \sim 10$. This result might represent a favourable feature in the investigation of the effect of atmospheric-like turbulence on bluff body aerodynamics. The expansion of the test section has a limited effect in the isotropy of turbulence, as the anisotropy indicates a light axialsymmetry. This result confirms that the quality of the turbulence flow field is comparable upstream and downstream of a slow variation in the cross-section of the wind tunnel.

3.3. Gaussianity

In homogeneous and isotropic turbulence, the probability distribution function is analogous to the normal distribution. This has been shown to hold true even for decaying grid generated turbulence (Wilczek et al., 2011). This means the skewness of the velocity components yields $S_u=S_v=S_w=0$ and the kurtosis $K_u=K_v=K_w=3$. The latter, in particular, only applies if the flow is purely gaussian.

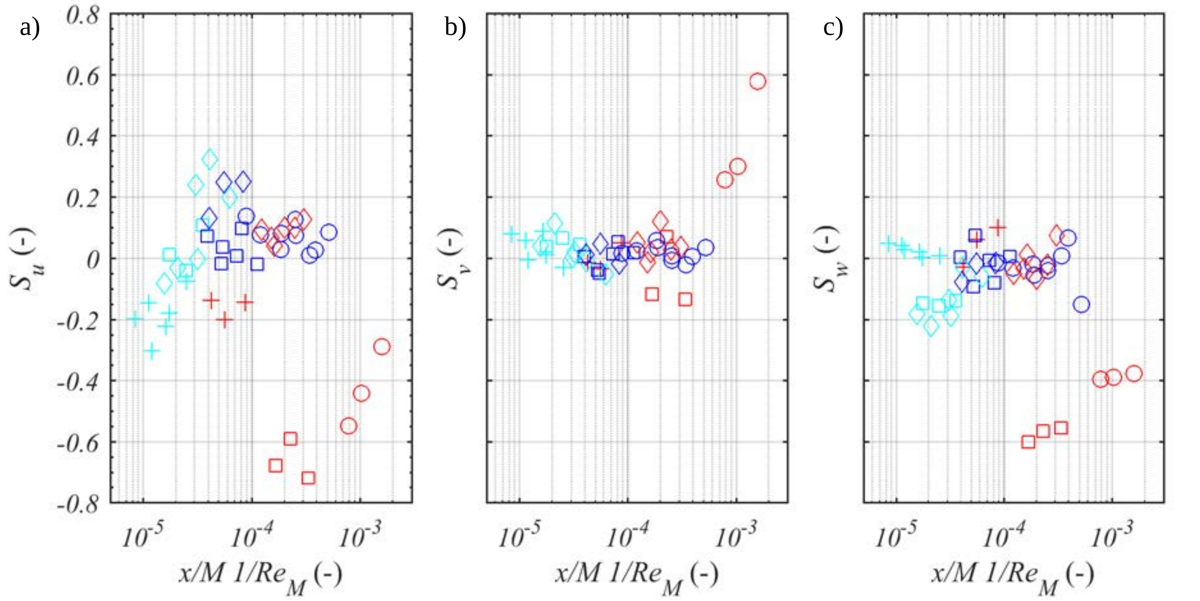

Figure 12 Skewness of velocity components for all grids and velocities. Colours after distance (Table 4).

The skewness of all components is plotted in Figure 12. Although a different behaviour is observed for the different grids, the skewness tends to become zero for $x/M>10$. The stream-wise component only seems affected by the distance, as data taken at $x/M<10$ shows to gradually converge towards zero. For grid #1, $S_u<0$ indicates an enhanced production of vorticity characteristic of a point in an oscillating or unstable shear layer. Arguably, this occurs due to the large mesh size, which in turn produces a non-uniform velocity cross-profile (Isaza et al., 2014). Data taken at $x\geq 9.1$ m differs from $S_u=0$. However, this only occurs for grids #2 and #3. Arguably, the lower β of grids #1 and #4 allows the near-field region characteristics to persist. This would also explain the negative values of S_u for grids #2 and #3 at $x/M<10$. The other components show a more pronounced gaussian behaviour, but $S_u\neq 0$ is observed after the expansion for grids #2 and #3.

The kurtosis (or flatness) of the flow is shown in Figure 13 for all components. The behaviour is more gaussian than for skewness, although after the expansion the data differs from $K_u=3$ for grids #2 and #3 after the expansion. K_v and K_w, unlike the skewness case, differ more than K_u for all ranges of data. These results are consistent with the anisotropy of the flow: the expansion stretches the vortices and it affects the isotropy of turbulence. Another possible explanation for the deviation from the normal distribution can be explained by a lack of flow homogeneity due to the particular grid arrangement. A lack in homogeneity causes the velocity field to be strained and it is believed this effect is also registered in the statistics (Mydlarski and Warhaft, 2006). The non-uniformity of the mean flow can be roughly assessed from Figure 7 b), where the change in the centreline value is plotted against distance. However, the uniformity of grid turbulence is a topic which would deserve a more thorough investigation (Carbó Molina et al., 2017).

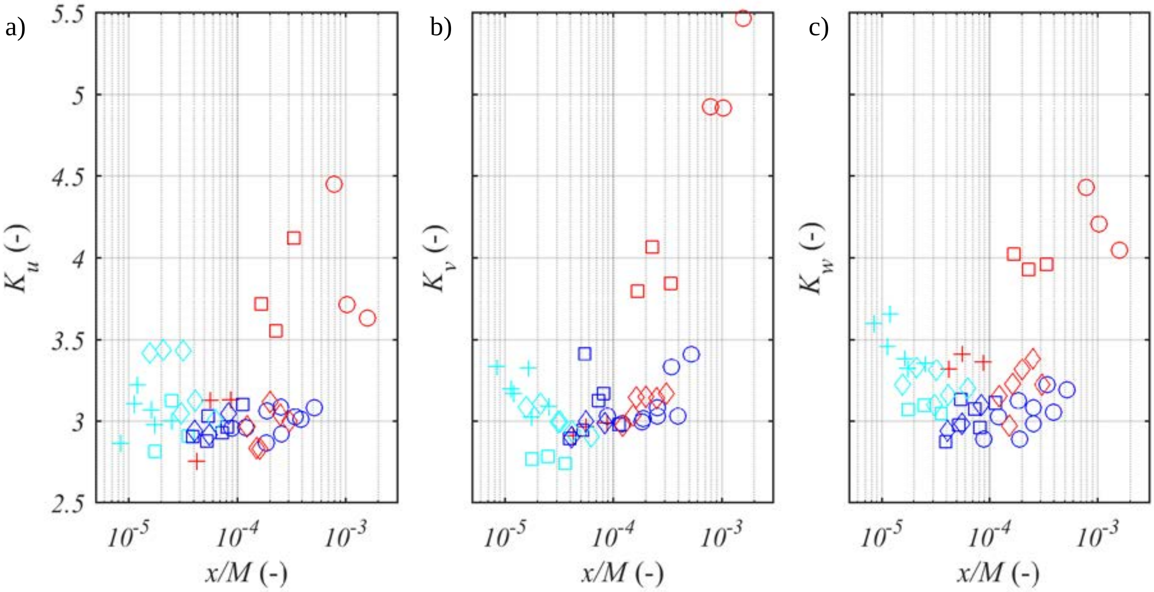

Figure 13 Kurtosis of velocity components for all grids and velocities. Colours after distance (Table 4).

3.4. Independently varied statistics

The use of a set of grids combined with an expansion section allows atmospheric-like highly isotropic turbulence to be reproduced, i.e. a flow field having I_u~$10\div15$ % and L_u~$25\div30$ cm. The study on the turbulence decay, which has been proposed in Section 3.1, can be used to plot a turbulence intensity versus integral length scale diagram. This defines a design chart, which is useful when choosing the needed turbulence characteristics. In Figure 14 a), a simple empirical relation is proposed to fit the data, which might be useful to design an experimental setup combined with an expansion. The proposed model is based on the summation of two power laws in the form of $f(x)=Ax^{-p}+Bx^{+n}$, where the negative power law is obtained from the least square fits of I_u and L_u, shown in Figure 4. A combination of the fits which holds for all grids is $I_u=0.025(L_u/M)^{-3/2}$, which is plotted in Figure 14 a). This curve is not able to model the effect of the expansion. Therefore, a second positive power law is summed to the fit of the data, and the following formula has been derived:

$$I_u=A\left[\left(\beta\frac{b}{M}\right)^2\left(\frac{L_u}{M}\right)^{-2}+\frac{B}{x_L}\left(\frac{L_u}{M}\right)^{\alpha}\right] \quad (12),$$

where $A=0.6$ and $B=1.5$ are two fitting constants, $\beta\, b/M = b/M\,(1\text{-}\,b/M)^2$ is a parameter based on the porosity of the grid, $x_L = 4/M$ is the expansion mesh distance, and $\alpha=1.45$ is the ratio of the expansion outlet and inlet cross section area $(2.5\times1.8)/(2\times1.5)$. Equation 12 is plotted in Figure 14 a) along with the least square fit of the data. With this simple model, the turbulence statistics found at the outlet of the expansion can be accurately estimated for grids #2, #3 and #4, while a significant mismatch is noticeable for grid #1, as expectable from previous results. The model is able to only estimate statistics straight at the outlet of the expansion section. For larger distances, no further conclusions can be made with this dataset. Equation 12 is then valid for $x_L>10$ and for $\beta>0.5$ only.

The fit proposed in Equation 12 is used to plot a dimensional design chart in Figure 14 b). The measured data is also plotted. Several alignments are found and plotted in the graph, where statistics can be varied independently of one another. In Figure 14 b), multiple points of interest are shown, where integral length scales up to *33cm* can be reached and a turbulence intensity of *15-16%* can be achieved. The use of an expansion test section has an important role in obtaining such a variation in the statistics, and it might allow for constant I_u and varying L_u to be obtained using a single grid, as it is particularly evident for grids #3 grid #2. However, grid #4 does not show the same behaviour, and turbulence intensity monotonically decreases due to the lower porosity. Although it behaves differently, grid #1 is also shown together with its least square fit. It seems that turbulence intensity can be substantially increased placing the grid at $x_L < 10$, which in turn does not affect substantially the quality of the flow field.

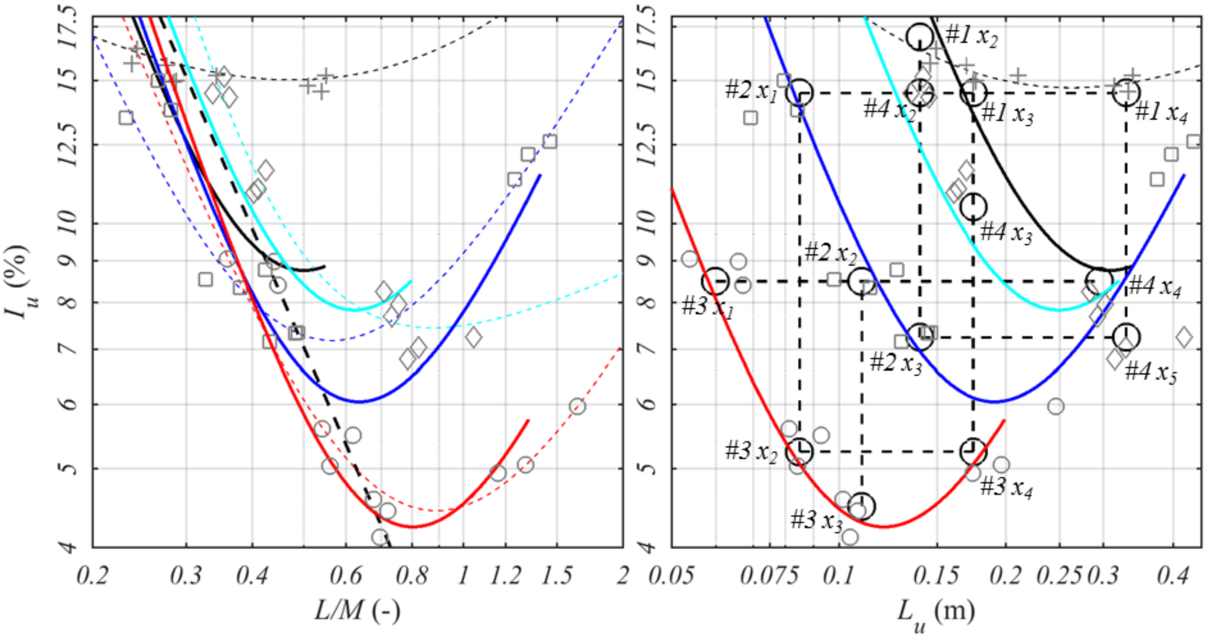

Figure 14 Turbulence Intensity versus Integral Length Scale of turbulence in a) non-dimensional, and b) dimensional form. Least square fit of all data (- -; - -; - -; - -; for grids #1, #2, #3 and #4, respectively), and of data at $x \leq 4$ m (- -) is plotted together with Equation 12 (—; —;—;— for grids #1, #2, #3 and #4, respectively). Circles and dashed black lines in b) refer to Table 5.

The statistics varied independently in Figure 14 need to show similar turbulence characteristics to be useful for wind tunnel tests. The Power Spectral Density (PSD) of the velocity measurements E_u is useful for this purpose. The spectra are estimated using the Welch overlapped segment FFT averaging technique. To reduce noise at higher frequencies, a Hanning window is used to split the signal into segments of length 0.6042 s, which is $1/100$th of the total realisation length of $u(t)$. The segments are overlapped by 50 %. The number of Discrete Fourier Transform (DFT) used in the PSD estimate is given by the greater of 2^8 or the first exponent of power of 2^n greater than the length of the overlapped segment, i.e. $1/2\ 0.6042$ s, which yields 151.05 Hz. This allows for a frequency step size of 3.33 Hz to be reached. A correction to exclude potential large scales from the wind tunnel was not necessary, as the turbulent flow characteristics in the empty wind tunnel test section are respectively: $L_u=0.013$ m, $\lambda_u=0.004$ m with $I_u=1.03$ %, $I_v=0.4$ %, $I_w=0.32$ % and $U=16.3$ m/s. The estimated PSD is fitted to the von Kármán formulation given in Equation 6, to give a comparison with atmospheric turbulence.

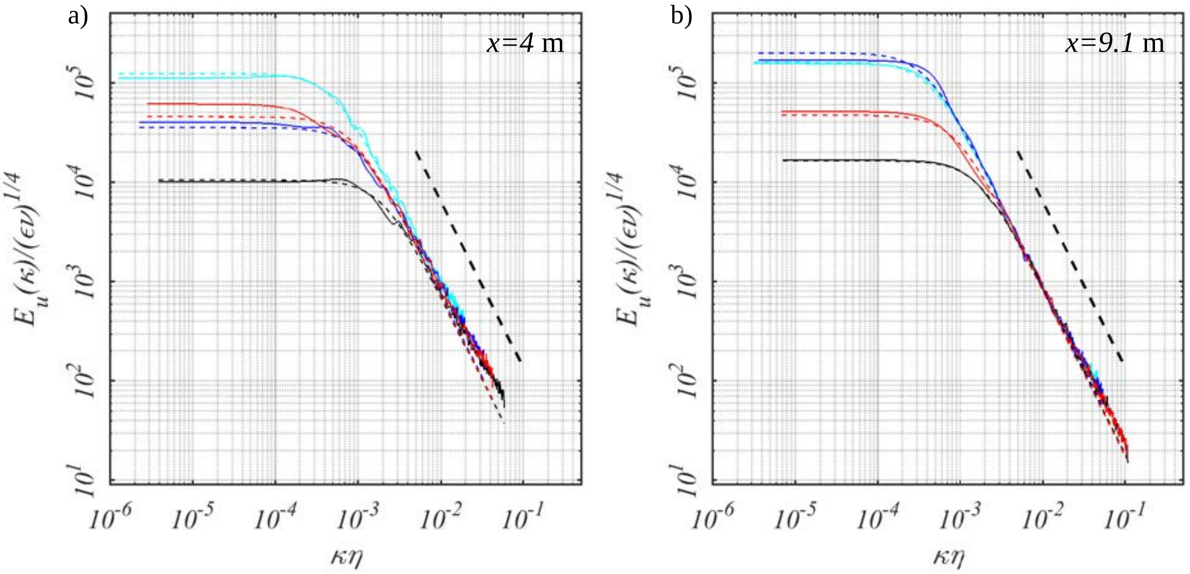

Figure 15 Wave number spectrum a) at the inlet of the expansion x= 4 m, and b) at the outlet x=9.1 m; Continuous line for grid #1 (—), #2 (—), #3 (—), and #4 (—); dashed line for von Kármán fitting; (- -) -5/3 power law.

The longitudinal wave number spectrum, non-dimensionalised using ε and η, is plotted in Figure 15 for measurements at the inlet (a) and at the outlet (b) of the expansion. This plot emphasizes the vicinity of the measurements with the *-5/3* power law for the inertial subrange of the spectrum. For comparison, the von Kármán fit is plotted with dashed lines. All grids show a close match with the -*5/3* law, consistently with previous results from literature (Isaza et al., 2014). This behaviour suggests that the isotropy and development of the energy cascade of the chosen experimental setup is not affected by the distance from the grid. A closer look might detect a slightly larger deviation from the -*5/3* law for data measured at $x \leq 4$ m, which could be interpreted as a contradiction to findings shown in Figure 11. However, this might depend on the low sampling rate used in the experiments (Roach, 1987).

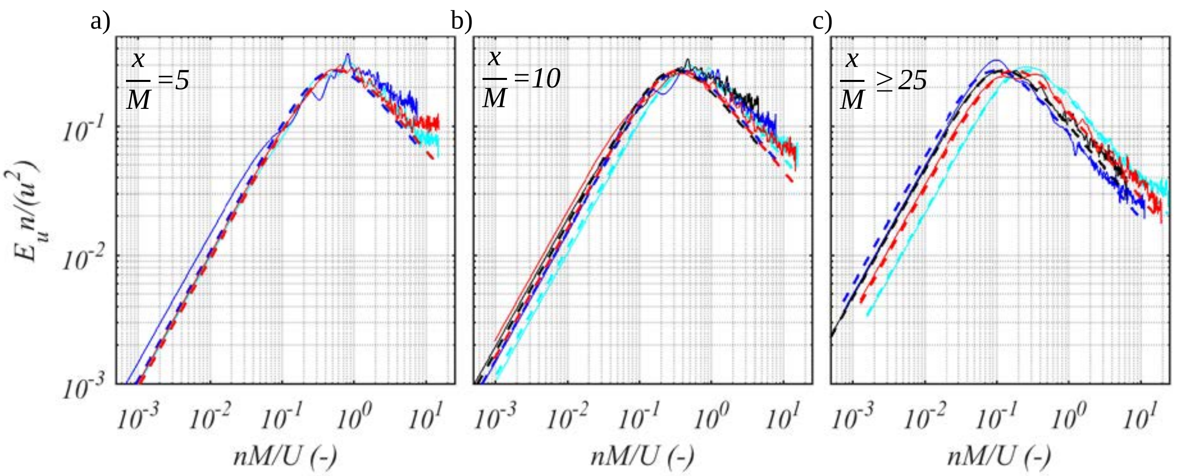

Figure 16. Power Spectral Density of turbulence for positions a) x/M =5, b) x/M=10 and c) x/M>25 and wind speed u_{rot}=15m/s. Continuous line for grid #1 —, #2 —, #3 —, and #4 —; dashed line for von Kármán fitting.

Nevertheless, the turbulence field is sufficiently developed and broad-banded for all distances, abnormal peaks in the spectra are absent, suggesting the absence of a residual effect of the bar wakes, even for small mesh distances, i.e. at *x/M~5*.

The evolution of the spectra with the mesh distance is reported in Figure 16. The spectra are non-dimensionalised using $E_u n/\overline{u^2}$ and nM/U and plotted at (a) *x/M=5*, (b) *x/M=10* and (c) *x/M>25* for all grids. Grid #1 is plotted at slightly different distances: (a) *x/M=5*, (b) *x/M=6.5*, and (c) *x/M=15*. Grid #2 is the only one in the setup, which deviates from the von Kármán fit more evidently at the low frequency end of the spectrum. Nevertheless, neither *x/M* or the expansion test section appear to affect the deviation of the statistics from theory. The PSD of the three components of velocity *u*, *v* and w is plotted in Figure 17 at *x=9.1* m. The vicinity to the von Kármán fit is analogous to that shown in Figure 16 and Figure 15.

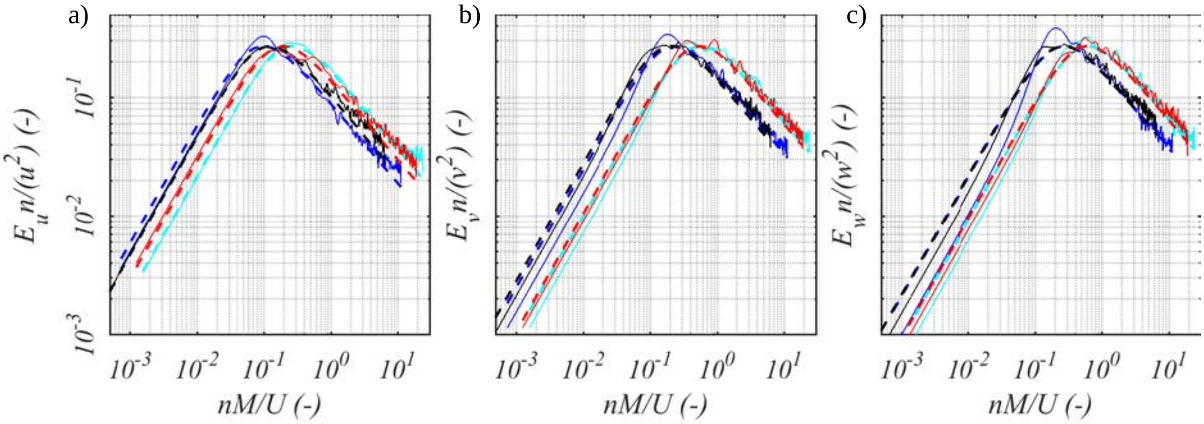

Figure 17 Non-dimensional PSD of all velocity components at x=9.1m and for u_r = 15m/s; Continuous line for grid #1 —, #2 —, #3 —, and #4 —; dashed line for von Kármán fitting.

The results confirm that the spectra maintain the properties of isotropy and uniformity as they are shown to have the same shape and easily fit with the von Kármán formulation. In Figure 18, the spectra are reported for statistics varied separately. Constant integral length scale associate with (a), (b), (c), and (d) plots, while constant turbulence intensity associate with (e), (f), (g), and (h). In the case of L_u, the maximum position of the spectra is located at the same frequency for a given scale, while for I_u the spectra are roughly overlapped at lower frequencies.

Table 5 Indepentely varied turbulence intensity and integral length scale, with relevant grid and position.

	Constant Integral Length Scale					*Constant Turbulence Intensity*			
Grid #(pos.) Figure 14b	*#3(x_2) #2(x_1)*	*#3(x_3) #2(x_2)*	*#2(x_3) #4(x_2) #1(x_2)*	*#3(x_4) #4(x_3) #1(x_3)*	*#4(x_5) #1(x_4)*	*#3(x_2) #3(x_4)*	*#2(x_3) #4(x_5)*	*#3(x_1) #2(x_2) #4(x_4)*	*#2(x_1) #4(x_2) #1(x_3) #1(x_4)*
Legend Figure 18	*a) —; —;*	*Not shown*	*b) —; —; —;*	*c) —; —; —;*	*d) —; —;*	*e) —; —;*	*f) —; —;*	*g) —; —; —;*	*h) —; —; —; —;*
L_u (m)	*0.085*	*0.11*	*0.145*	*0.175*	*0.33*	*0.09 0.175*	*0.165 0.33*	*0.065 0.11 0.29*	*0.08 0.135 0.175 0.33*
I_u (%)	*5.5 15*	*4.5 8.3*	*7.25 14.5 15.7*	*5.0 11.0 14.75*	*7.0 14.75*	*5.25*	*7.25*	*8.5*	*14.75*

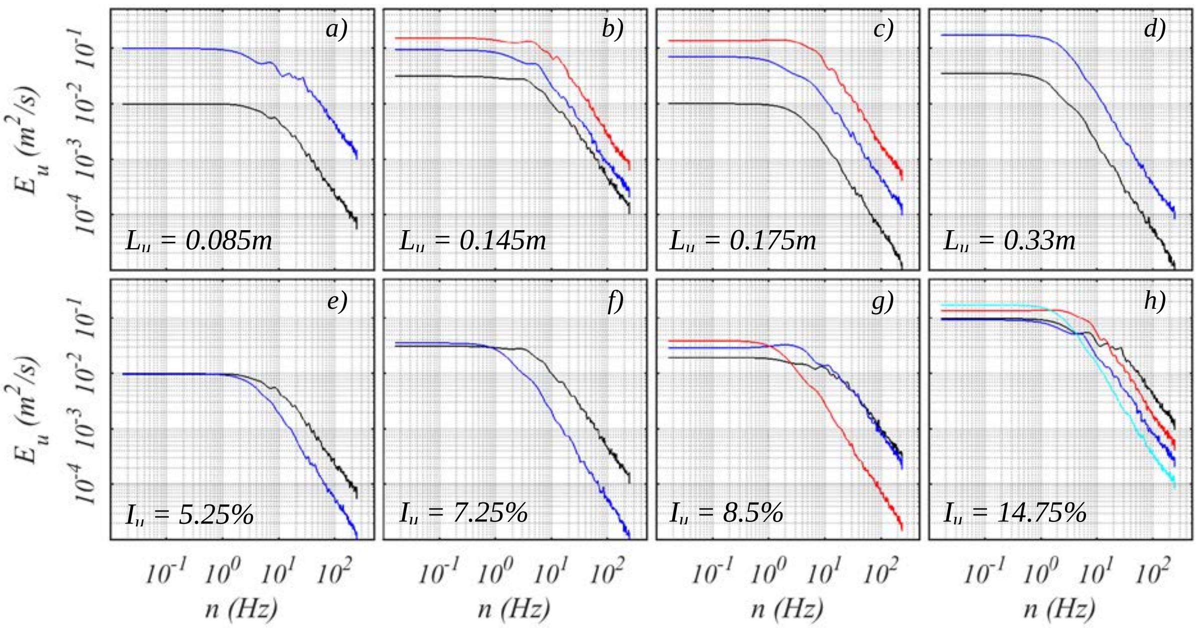

Figure 18. Power Spectral Density of velocity for constant integral length scale (a, b, c, d) and turbulence intensity (e, f, g, h); Colours as reported in Table 5.

4. Conclusions

The effect of an expansion test section on the turbulence characteristics of grid generated turbulence has been addressed in this study. To the knowledge of the authors, such a setup has not been discussed in literature. Results of measurements of the turbulent flow taken downstream of the expansion suggest following conclusions:

- A decrease of the mean velocity downstream of the expansion occurs due to the Venturi effect.
- Due to the change in the mean velocity, the turbulence intensity downstream of the expansion recovers to upstream values, instead of decaying proportionally to the distance.
- The stretching of vortices in the expansion also acts on the integral length scale, which is approximately doubled from what is normally encountered in literature.
- The flow behaviour changes from a pure isotropic one, to a slightly axisymmetric one.
- For lower porosity, the turbulence decay deviates less markedly from literature.
- The Taylor microscale is insensitive to the presence of the expansion, as dissipation remains the main phenomenon involved in the turbulence decay.
- Velocity Skewness and Kurtosis deviate from the normal distribution due to the expansion for lower grid drags for higher porosity.
- The energy spectra fit well to the von Kármán formulation downstream of the expansion, although a limited effect on the slope of the inertial sub-range is noticeable.

The possibility of separately varying both turbulence intensity and integral length scale has also been discussed with reference to the quality of the turbulent field. The flow field is acceptably close to the theoretical behaviour of homogeneous and isotropic turbulence throughout the measurements. The following conclusions can be made regarding grid generated turbulence as measured in this study:

- The near-field region is located at distances less than *x/M<5*, as for *x/M~5* the flow is found to be fully developed and dissipation only drives the decay of turbulence.
- The flow field is broadly Gaussian. This feature persists with distance and Reynolds number. However, some form of anisotropy occurs for values at *x/M<10*, which confirms that uniformity is a difficult property of the flow field to be achieved. This is a feature worth further investigation.
- Flow field statistics varied independently have shown similar behaviour against isotropy, gaussianity or the turbulence decay. The expansion is of great help in achieving a turbulent flow field with large integral length scale combined with high turbulence intensity, which otherwise would require closeness of measurements to grids with large bar size, i.e. to take measurements in the near-field region of the flow, where dissipation is not the main driver of turbulence decay.

Some limitations of grid turbulence generation can be overcome by modifying the cross section of the wind tunnel. The turbulent flow field is easily fitted to the von Kármán formulation for all distances, grids and combinations considered. Therefore, this technique is suggested to reproduce atmospheric turbulence conditions for the study of the effect of free stream turbulence for a variety of aerodynamic applications, such as wind energy harvesting.

Acknowledgments

The authors acknowledge the support of the European Commission's Framework Program "Horizon 2020", through the Marie Skodowska-Curie Innovative Training Networks (ITN) "AEOLUS4FUTURE - Efficient harvesting of the wind energy" (H2020-MSCA-ITN-2014: Grant agreement no. 643167) to the present research project.

Also, the Cost Action TU1804 WinerCost – “Wind Energy to enhance the concept of Smart cities” is gratefully acknowledged, for providing the possibility of a Short Term Scientific Mission, used to conduct this experiment.

A special thank goes to François Rigo for taking part in the construction of the setup and the run of the experiment, and to Arnaud Fabbri for the provision of the material for the construction of the grids.

References

Antoniou, I., Asimakopoulos, D., Fragoulis, A., Kotronaros, A., Lalas, D.P., Panourgias, I., 1992. Turbulence measurements on top of a steep hill. J. Wind Eng. Ind. Aerodyn. 39, 343–355.

Arie, M., Kiya, M., Suzuki, Y., Hagino, M., Takahashi, K., 1981. Characteristics of Circular Cylinders in Turbulent Flows. Bull. Japan Soc. Mech. Eng. 24, 640–647.

Baines, W.D., Peterson, E.G., 1951. An investigation of flow through screens. Trans. ASME 73, 467–80.

Banerjee, S., Krahl, R., Durst, F., Zenger, C., 2007. Presentation of anisotropy properties of turbulence, invariants versus eigenvalue approaches. J. Turbul. 8, N32.

Batchelor, G.K., 1946. The Theory of Axisymmetric Turbulence. Proc. R. Soc. A Math. Phys. Eng. Sci. 186, 480–502.

Batchelor, G.K., 1953. The Theory of Homogeneous Turbulence. Cambridge University Press.

Bearman, P.W., Morel, T., 1983. Effect of free stream turbulence on the flow around bluff bodies. Prog. Aerosp. Sci. 20, 97–123.

Bereketab, S., Wang, H.-W., Mish, P., Devenport, W.J., 2000. The Surface Pressure Response of a NACA 0015 Airfoil Immersed in Grid Turbulence. Volume 1; Characteristics of the Turbulence.

Bradshaw, P., Pankhurst, R.C., 1964. The design of low-speed wind tunnels. Prog. Aerosp. Sci. 5, 1–69.

Brzek, B., Torres-Nieves, S., Lebrón, J., Cal, R., Meneveau, C., Castillo, L., 2009. Effects of free-stream turbulence on rough surface turbulent boundary layers. J. Fluid Mech. 635, 207.

Cal, R.B., Lebrón, J., Castillo, L., Kang, H.S., Meneveau, C., 2010. Experimental study of the horizontally averaged flow structure in a model wind-turbine array boundary layer. J. Renew. Sustain. Energy 2, 13106.

Carbó Molina, A., Bartoli, G., De Troyer, T., 2017. Wind Tunnel testing of small Vertical-Axis Wind Turbines in Turbulent Flows. In: Procedia Engineering, X International Conference on Structural Dynamics, EURODYN 2017. Elsevier, Rome, pp. 3176–3181.

Cekli, H.E., van de Water, W., 2010. Tailoring turbulence with an active grid. Exp. Fluids 49, 409–416.

Comte-Bellot, G., Corrsin, S., 1966. The use of a contraction to improve the isotropy of grid-generated turbulence. J. Fluid Mech. 25, 657.

Conan, B., 2012. Wind resource accessment in complex terrain by wind tunnel modelling. Orléans.

Davidson, P.A., 2004. Turbulence: An Introduction for Scientists and Engineers. OUP Oxford.

de Karman, T., Howarth, L., 1938. On the Statistical Theory of Isotropic Turbulence. Proc. R. Soc. London A Math. Phys. Eng. Sci. 164.

Frenkiel, F.N., Klebanoff, P.S., Huang, T.T., 1979. Grid turbulence in air and water. Phys. Fluids 22, 1606.

Gartshore, I., 1984. Some effects of upstream turbulence on the unsteady lift forces imposed on prismatic two dimensional bodies. J. Fluids Eng.

George, W.K., 1992. The decay of homogeneous isotropic turbulence. Phys. Fluids A Fluid Dyn. 4, 1492–1509.

George, W.K., 2012. Asymptotic Effect of Initial and Upstream Conditions on Turbulence. J. Fluids Eng. 134, 61203.

Geyer, T.F., Sarradj, E., Hobracht, M., 2016. Noise generated by a leading edge in anisotropic turbulence. In: 45th International Congress on Noise Control Engineering (Inter.noise 2016). Hamburg.

Hancock, P.E., Bradshaw, P., 1983. The Effect of Free-Stream Turbulence on Turbulent Boundary Layers. J. Fluids Eng. 105, 284.

Hinze, J.O., 1975. Turbulence. McGraw-Hill.

Hoffmann, J.A., 1981. Effects of Free-Stream Turbulence on Diffuser Performance. J. Fluids Eng. 103, 385.

Hurst, D., Vassilicos, J.C., 2007. Scalings and decay of fractal-generated turbulence. Phys. Fluids 19, 35103.

Hussein, H.J., Capp, S.P., George, W.K., 1994. Velocity measurements in a high-Reynolds-number, momentum-conserving, axisymmetric, turbulent jet. J. Fluid Mech. 258, 31.

Isaza, J.C., Salazar, R., Warhaft, Z., 2014. On grid-generated turbulence in the near- and far field regions. J. Fluid Mech. 753, 402–426.

Jovanović, J., 2004. The Statistical Dynamics of Turbulence. Springer-Verlag, Berlin, Heidelberg, New York.

Kaimal, J.C., Wyngaard, J.C., Haugen, D.A., Coté, O.R., Izumi, Y., Caughey, S.J., Readings, C.J., 1976. Turbulence Structure in the Convective Boundary Layer. J. Atmos. Sci.

Kang, H.S., Chester, S., Meneveau, C., 2003. Decaying turbulence in an active-grid-generated flow and comparisons with large-eddy simulation. J. Fluid Mech. 480, 129–160.

Kim, J.W., Haeri, S., Joseph, P.F., 2016. On the reduction of aerofoil–turbulence interaction noise associated with wavy leading edges. J. Fluid Mech. 792, 526–552.

Kistler, A.L., Vrebalovich, T., 2006. Grid turbulence at large Reynolds numbers. J. Fluid Mech. 26, 37.

Kurian, T., Fransson, J.H.M., 2009. Grid-generated turbulence revisited. Fluid Dyn. Res. 41, 21403.

Laneville, A., 1973. Effects of turbulence on wind-induced vibrations of bluff cylinders. University of British Columbia, Vancouver, Canada.

Larssen, J. V., Devenport, W.J., 2011. On the generation of large-scale homogeneous turbulence. Exp. Fluids 50, 1207–1223.

Lee, B.E., 1975. Some effects of turbulence scale on the mean forces on a bluff body. J. Wind Eng. Ind. Aerodyn. 1, 361–370.
Lumley, J.L., 1979. Computational Modeling of Turbulent Flows. Adv. Appl. Mech. 18, 123–176.
Makita, H., 1991. Realization of a large-scale turbulence field in a small wind tunnel. Fluid Dyn. Res. 8, 53–64.
Makita, H., Sassa, K., 1991. Active Turbulence Generation in a Laboratory Wind Tunnel. In: Johansson, A. V, Alfredsson, P.H. (Eds.), Advances in Turbulence 3: Proceedings of the Third European Turbulence Conference Stockholm, July 3--6, 1990. Springer Berlin Heidelberg, Berlin, Heidelberg, pp. 497–505.
Maldonado, V., Castillo, L., Thormann, A., Meneveau, C., 2015. The role of free stream turbulence with large integral scale on the aerodynamic performance of an experimental low Reynolds number S809 wind turbine blade. J. Wind Eng. Ind. Aerodyn. 142, 246–257.
Mehta, R.D., 1979. The aerodynamic design of blower tunnels with wide-angle diffusers. Prog. Aerosp. Sci. 18, 59–120.
Melina, G., Bruce, P.J.K., Vassilicos, J.C., 2016. Vortex shedding effects in grid-generated turbulence. Phys. Rev. Fluids 1, 44402.
Mish, P.F., Devenport, W.J., 2006. An experimental investigation of unsteady surface pressure on an airfoil in turbulence—Part 1: Effects of mean loading. J. Sound Vib. 296, 417–446.
Mohamed, M.S., Larue, J.C., 1990. The decay power law in grid-generated turbulence. J. Fluid Mech. 219, 195.
Morenko, I. V., Fedyaev, V.L., 2017. Influence of turbulence intensity and turbulence length scale on the drag, lift and heat transfer of a circular cylinder. China Ocean Eng. 31, 357–363.
Mydlarski, L., Warhaft, Z., 2006. On the onset of high-Reynolds-number grid-generated wind tunnel turbulence. J. Fluid Mech. 320, 331.
Nakamura, Y., 1993. Bluff-body aerodynamics and turbulence. J. Wind Eng. Ind. Aerodyn. 49, 65–78.
Nakamura, Y., Ohya, Y., Ozono, S., 1988. The effects of turbulence on bluff-body mean flow. J. Wind Eng. Ind. Aerodyn. 28, 251–259.
Nedić, J., Vassilicos, J.C., 2015. Vortex Shedding and Aerodynamic Performance of Airfoil with Multiscale Trailing-Edge Modifications. AIAA J. 53, 3240–3250.
Peyrin, F., Kondjoyan, A., 2002. Effect of turbulent integral length scale on heat transfer around a circular cylinder placed cross to an air flow. Exp. Therm. Fluid Sci. 26, 455–460.
Pope, S.B., 2000. Turbulent Flows, Cambridge University Press.
Roach, P.E., 1987. The generation of nearly isotropic turbulence by means of grids. Int. J. Heat Fluid Flow 8, 82–92.
Saathoff, P.J., Melbourne, W.H., 1997. Effects of free-stream turbulence on surface pressure fluctuations in a separation bubble. J. Fluid Mech. 337, S0022112096004594.
Seoud, R.E., Vassilicos, J.C., 2007. Dissipation and decay of fractal-generated turbulence. Phys. Fluids 19, 105108.
Sicot, C., Devinant, P., Loyer, S., Hureau, J., 2008. Rotational and turbulence effects on a wind turbine blade. Investigation of the stall mechanisms. J. Wind Eng. Ind. Aerodyn. 96, 1320–1331.
Simmons, L.F.G., Salter, C., 1934. Experimental Investigation and Analysis of the Velocity Variations in Turbulent Flow. Proc. R. Soc. London A Math. Phys. Eng. Sci. 145.
Sreenivasan, K.R., 1995. On the universality of the Kolmogorov constant. Phys. Fluids 7, 2778–2784.
Sreenivasan, K.R., Antonia, R.A., 1997. THE PHENOMENOLOGY OF SMALL-SCALE TURBULENCE. Annu. Rev. Fluid Mech 29, 435–72.
Swalwell, K., Sheridan, J., Melbourne, W., 2004. The effect of turbulence intensity on performance of a NACA 4421 airfoil section. 42nd AIAA Aerosp.
Taylor, G.I., 1935. Statistical Theory of Turbulence. Proc. R. Soc. London A Math. Phys. Eng. Sci. 151.
Uberoi, M.S., 1956. Effect of Wind-Tunnel Contraction on Free-Stream Turbulence. J. Aeronaut. Sci. 23, 754–764.
Vickery, B.J., 1966. Fluctuating lift and drag on a long cylinder of square cross-section in a smooth and in a turbulent stream. J. Fluid Mech. 25, 481.
Wang, S., Zhou, Y., Alam, M.M., Yang, H., 2014. Turbulent intensity and Reynolds number effects

on an airfoil at low Reynolds numbers. Phys. Fluids 26, 115107.
Wilczek, M., Daitche, A., Friedrich, R., 2011. On the velocity distribution in homogeneous isotropic turbulence: correlations and deviations from Gaussianity. J. Fluid Mech. 676, 191–217.
Younis, N., Ting, D.S.K., 2012. The subtle effect of integral scale on the drag of a circular cylinder in turbulent cross flow. Wind Struct. 15, 463–480.